C. R. Mecanique 345 (2017) 690–705

Contents lists available at ScienceDirect

Comptes Rendus Mecanique

www.sciencedirect.com

Numerical analysis of the effects induced by normal faults and dip angles on rock bursts

Lishuai Jiang [a,1], Pu Wang [a,*,1], Peipeng Zhang [b], Pengqiang Zheng [b], Bin Xu [a]

[a] State Key Laboratory of Mining Disaster Prevention and Control Co-founded by Shandong Province and the Ministry of Science and Technology, Shandong University of Science and Technology, Qingdao 266590, China
[b] Department of Resources and Civil Engineering, Shandong University of Science and Technology, Tai'an 271000, China

ARTICLE INFO

Article history:
Received 16 January 2017
Accepted 21 June 2017
Available online 12 July 2017

Keywords:
Normal fault
Dip angle of a fault
Strata behaviors
Instability of a fault
Rock burst

ABSTRACT

The study of mining effects under the influences of a normal fault and its dip angle is significant for the prediction and prevention of rock bursts. Based on the geological conditions of panel 2301N in a coalmine, the evolution laws of the strata behaviors of the working face affected by a fault and the instability of the fault induced by mining operations with the working face of the footwall and hanging wall advancing towards a normal fault are studied using UDEC numerical simulation. The mechanism that induces rock burst is revealed, and the influence characteristics of the fault dip angle are analyzed. The results of the numerical simulation are verified by conducting a case study regarding the microseismic events. The results of this study serve as a reference for the prediction of rock bursts and their classification into hazardous areas under similar conditions.

1. Introduction

Because of the increase in the number of coal-mining activities and the depth of mining, geological conditions are becoming gradually more complex in East China, North China, Central China, and Southwest China. The complex geological conditions lead to dynamic disasters such as coal and gas outbursts, rock bursts, and shock bumps [1,2]. Several on-site observations show that rock bursts are easily induced in the vicinity of faults, fold belts, angle variation belts of coal seam, etc. [3–5]. Hence, faults are the most common causes of rock burst, the influence of which is considerable because of the discontinuity of the rocks cut by the fault. Fig. 1 shows several on-site images taken after two rock bursts that occurred in the Jining No. 3 coalmine in 2004 (affected by the fault marked as SF28) and Qianqiu coalmine in 2011 (affected by the fault marked as F16). These rock bursts can lead to serious problems such as ejection of rocks and coal, damage of supports, overturning of devices, and even fatalities [6,7].

The overall structures of many mining areas in China are relatively simple, largely exhibiting small and medium normal faults [8,9]. Hence, in this study, the effects of a normal fault on mining in front of a working face are studied. With regard to the formation mechanism of the faults [10,11], there is no compressive deformation in the two walls of the normal fault; moreover, the elastic strain energy does not accumulate because most of the normal faults are tensional in nature, which are due to the vertical compressive load [8]. The results of an in situ stress test show that partial or full energy accumulated

* Corresponding author.
E-mail address: 15854848872@163.com (P. Wang).
[1] The two authors contributed equally to this paper.

http://dx.doi.org/10.1016/j.crme.2017.06.009
1631-0721/

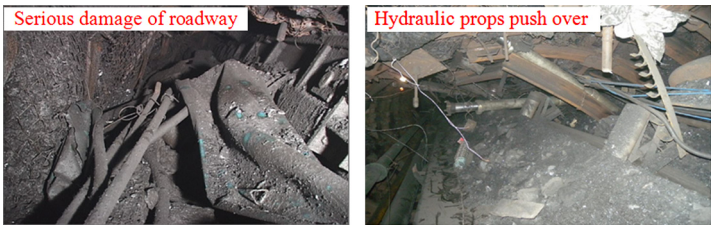

Fig. 1. On-site images after rock burst accidents in Jining No. 3 coalmine and Qianqiu coalmine.

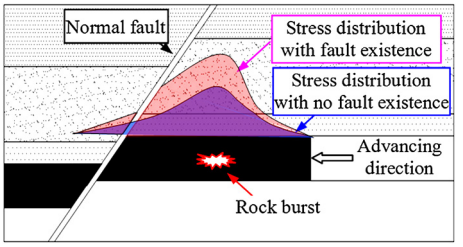

Fig. 2. Sketch map of rock burst induced by concentrated stress affected by normal faulting.

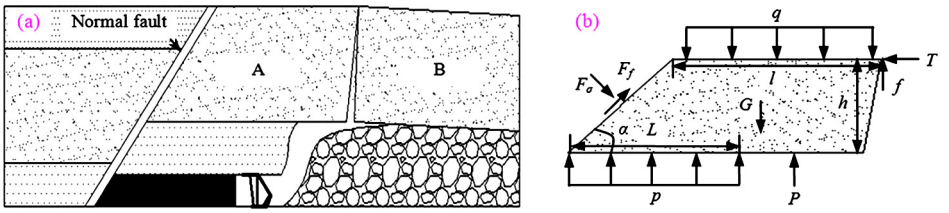

Fig. 3. Mechanical analysis of roof rock near the fault. (a) Roof structure, and (b) mechanical analysis model of block A.

in the rocks is released when the rocks are destroyed, and subsequently, the tectonic stress partly or completely disappears [12]. Hence, the mechanism of the rock burst induced by a normal fault largely involves mining concentrated stress and roof subsidence. Fig. 2 shows the distribution maps of a rock burst induced by the concentrated stress due to a normal fault.

With the working face approaching the fault, the abutment stress is concentrated notably on the fault coal pillar because of the discontinuity in the stress distribution induced by the cutting of the fault; moreover, the roof rocks exhibit large-scaled movement. In particular, the probability of a rock burst is considerable if the stratum is hard and thick because more energy is released (including the elastic strain energy of the coal body and the kinetic energy transformed from static energy) during subsidence. The fault activation is affected by mining operations, leading to a rock burst because the fault is unstable and tends to slip. Hence, the effects of the strata behaviors of the working face due to the fault and the instability of the fault induced by the mining operations are of paramount importance with respect to rock bursts.

The roof near the fault moves along the fault instead of forming a new fracture because of the cutting of the fault [12]. Fig. 3a shows the roof structure during the mining of the footwall. The hard roof block marked as A is used as the research object. This block bears the resultant action of the overlying uniform load, deadweight, holding power of the coal body, holding power of the hydraulic support, horizontal pressure exerted by block B, friction between the blocks A and B, normal pressure exerted by the other wall rocks of the fault, and friction between two fault walls, as shown in Fig. 3b.

By employing the equilibrium conditions $\sum F_x = 0$ and $\sum F_y = 0$, Eq. (1) is obtained as follows:

$$\begin{cases} F_\sigma \cdot \sin\alpha + F_f \cdot \cos\alpha - T = 0 \\ ql + G + F_\sigma \cdot \cos\alpha - F_f \cdot \sin\alpha - f - pL - P = 0 \end{cases} \tag{1}$$

$$F_\sigma = \sigma h / \sin\alpha, \qquad f = \mu T \tag{2}$$

where q is the overlying uniform load, N/m; p is the uniform load exerted by the coal body, N/m; σ is the normal stress of the fault plane, N/m; G is the deadweight of the hard roof block A, N; T is the horizontal pressure exerted by block B, N; f is the friction between the blocks A and B, which is determined using T, N; P is the holding power of the hydraulic support, N; F_σ is the normal pressure exerted by the other wall rocks, N; F_f is the friction between the two fault walls, N; μ is the friction factor; α is the dip angle of the fault; l is the length of the uniformly distributed load, m; L is the distance between the working face and the fault, m; and h is the thickness of the block A, m.

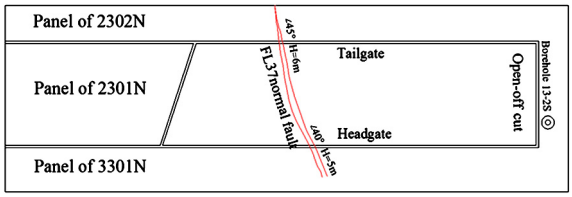

Fig. 4. Geological conditions of panel 2301N.

Eq. (3), which expresses the critical condition of the roof movement, is obtained using Eqs. (1) and (2) as follows:

$$ql + G - pL - P - \frac{2\sigma h}{\sin 2\alpha} - (\mu + \tan\alpha)T = 0 \tag{3}$$

As expressed in Eq. (3), the roof movement is affected by the dip angle of the normal fault and so do the rock bursts near the fault.

With regard to the occurrence of the fault, many studies have been conducted regarding the characteristics of strata behaviors and the factors that induce rock bursts near the fault using different methods. The mine stress distribution of the working face or roadway near the fault and its influence on the roof stability due to the fault were studied. The causes and mechanisms of rock bursts were analyzed in terms of the geological structure, seismic activity, and stress field. The effects of the physical and mechanical properties of the fault and the roof on the rock burst are obtained using numerical simulation [13–20]. The laws of the strata behaviors or the fault slipping near the fault were studied using a physical simulation. Moreover, a reliable basis for the prediction and prevention of rock bursts near the fault was provided [21–26]. The Voussoir beam model and the fold-catastrophe model were established based on the theoretical analyses of the Voussoir beam theory and the shear-strain gradient plasticity theory and energy criterion. The instability criterion of the fault band and elastic rock system was proposed, and the influence factors of rock bursts due to faults were analyzed [24,27–30].

Many studies have been conducted on the characteristics of strata behaviors or on the mechanical mechanism of fault slipping; however, the influence of mining was often neglected. In fact, the dynamic disasters such as rock bursts are usually induced by mining activities. Hence, in this study, the strata behaviors of the working face affected by the fault and the stability of a fault induced by the mining operations are discussed.

Frequently used methods include on-site observation, theoretical calculation, and simulation analysis. It is difficult to accurately obtain the universal laws using on-site observation because the rock bursts are concealed. The theoretical calculation generally involves summarizing the universal laws based on a simplified mechanical model; however, it is difficult to find a suitable mechanical model to solve the dynamic problems due to rock bursts. The physical and numerical simulations can be employed to change the test conditions at will; however, the former requires a large input and a long cycle in the repeated tests conducted to change the dip angle of the fault. Nevertheless, in the latter method, a constitutive model of the software is used to simulate the different dip angles of the fault, which is convenient and effective; moreover, the method requires only a short cycle and less input [31–33]. Hence, the numerical simulation is an effective method to solve the complex problem observed in underground mines.

In this study, two numerical models are established with different mining sequences toward the fault using the UDEC simulation software based on the geological conditions of panel 2301N in Xinjulong coalmine. Subsequently, the evolution laws of the strata behaviors of the working face affected by the fault and the instability of the fault induced by the mining operations are compared and analyzed. Further, the influence of different dip angles of the fault on the rock burst is determined by changing the dip angle of the fault, which serves as a reference for the prevention of rock bursts and its division of hazardous areas under similar conditions.

2. Engineering background

2.1. Geological conditions of panel 2301N

The panel 2301N is the northern first mining fully mechanized top coal-caving face of the second district in the Xinjulong coalmine. The mining depth is in the range of 700–820 m. The average thickness and dip angle of the coal seam, which has a weak bursting liability, are 9.2 m and 3°, respectively. The length and strike length of the working face are 270 m and 1597 m, respectively. A normal fault, $\angle 45°$ $H = 6$ m and $\angle 40°$ $H = 5$ m (H represents the fall height of the fault) and marked as FL37, occurs in front of the open-off cut with the distance of 625 m, as shown in Fig. 4. The strata revealed by the borehole marked as 13–2S near the fault contain sandstone and mudstone, which have medium bursting liability. Table 1 presents the lithology and thickness of the strata.

2.2. Microseismic events of panel 2301N

The microseismic activities are an important indicator for detecting burst-prone areas, and their locations vary based on the progression of mining activities [34]. Microseismic monitoring systems are widely employed to estimate the locations

Table 1
Lithologies and thicknesses of the roof and floor of panel 2301N.

Sequences	Lithology	Thickness (m)	Sequences	Lithology	Thickness (m)	Sequences	Lithology	Thickness (m)
R9	Claystone	17.5	R5	Packsand	5.15	R1	Siltstone	2.74
R8	Mudsotne	13.3	R4	Medium sand	5.45	Coal	Coal	9.5
R7	Sandy mudstone	8.24	R3	Mudsotne	3.76	F1	Siltstone	12.12
R6	Siltstone	6.16	R2	Packsand	18.5	F2	Packsand	20

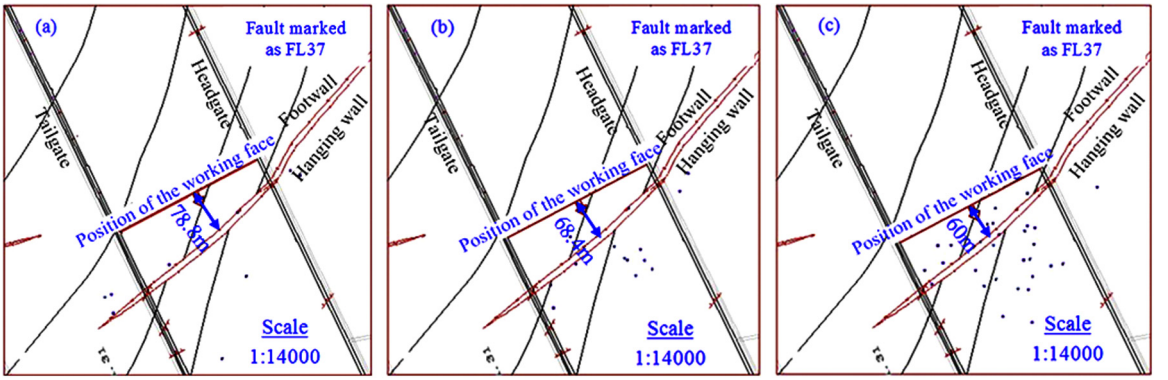

Fig. 5. Plane projection charts of microseismic events at working face [37]. (a) October 23, 2013, (b) October 25, 2013, and (c) October 27, 2013.

of microseismic events occurring in underground mines by recording waveforms [35,36]. The high-precision microseismic monitoring system developed by the University of Science & Technology Beijing was installed and is in operation in Xinjulong coalmine. The microseismic signal provided real-time monitoring for events of energy signals exceeding 10^2 J, in the frequency range of 1–1500 Hz, and less than 110 dB. The measurement accuracy is greater than 95%. The system mainly comprises a real-time monitoring recorder, geophones, an analyzer, and a digital transmission system. The microseismic events that occur in panel 2301N are recorded using a system comprising at least 12 geophones with a frequency range of 30–1500 Hz, which is installed along the advancing direction from the open-off cut in the tailgate and headgate, with an interval of 50 m. The signals are relayed with a maximum data transmission rate of 10 MB/s. The broadband and moving-coil type geophones are employed with a resonance frequency of 4.5 Hz. The geophones are removed and moved forward in a timely manner with the advancement of the working face. Moreover, more than six geophones for each roadway are ensured to work regularly [37].

The mining on panel 2301N commenced on July 5, 2013 and the mining activity completed on May 19, 2014. The following microseismic monitoring dates and the corresponding distance between the working face and the fault are selected: 78.8 m (October 23, 2013), 68.4 m (October 25, 2013), and 60 m (October 27, 2013). This distance is the linear distance from the middle of the working face to the fault. Fig. 5 shows the spatial distribution on the plane. In the figure, the black dots represent the microseismic events.

As shown in Fig. 5, with the gradual advancement of panel 2301N, there is a gradual increase in the number of microseismic events, primarily concentrated near the fault. It is indicated that the microseismic events are affected by the fault and the effect increases gradually. From Figs. 5a and 5b, when the distances between the working face and the fault are 78.8 m and 68.4 m, only a few microseismic events are observed near the fault because the large fault coal pillar on the footwall cut by the fault still has a strong bearing capacity with respect to the high concentrated stress. As shown in Fig. 5c, when the distance decreases to 60 m, there is an increase in the number of microseismic events, which might be because of the plastic failure of the fault coal pillar on the footwall with the decreases in the width and bearing capacity of the coal pillar. Therefore, the evolution laws of the strata behaviors and fault instability significantly affect the relationship between the dynamic phenomena, such as rock bursts and microseismic activity, and mining activities.

3. Evolution laws of strata behaviors of working face affected by fault

3.1. Establishment of UDEC numerical model

The numerical simulation methods, which are widely used in engineering and theoretical analysis, can be used to effectively solve complex engineering problems. The UDEC software is a two-dimensional discrete element calculation program for discontinuous media, which is suitable for simulating a discontinuous block set of joints or structural planes. Thus, it is able to meet the needs of this study [38,39]. Based on the geological conditions of panel 2301N, a UDEC numerical model is established concerning the working face and a normal fault.

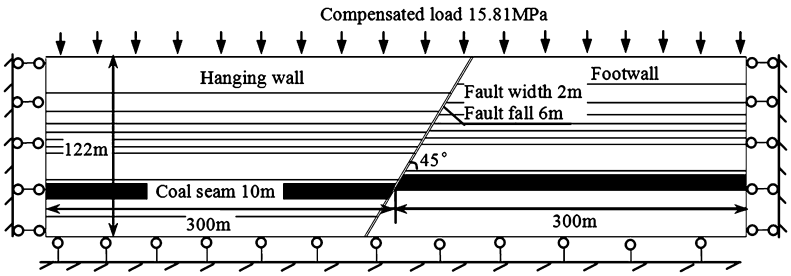

Fig. 6. Numerical calculation model.

Table 2
Mechanical properties of rock masses.

Lithology	Thickness (m)	Shear (GPa)	Bulk (GPa)	Density ($kg \cdot m^{-3}$)	Tensile strength (MPa)	Cohesion (MPa)	Internal friction angle (°)
Claystone	18	0.65	1.41	2400	0.15	0.7	32
Mudsotne	13	1.85	2.67	2400	2.19	0.8	33
Sandy mudstone	8	2.14	3.26	2500	1.15	0.7	33
Siltstone	6	4.65	6.41	2600	2.56	1.0	32
Packsand	5	15.40	21.60	2700	3.15	7.1	37
Medium sand	5	13.85	16.29	2500	2.35	5.3	35
Mudsotne	4	2.95	4.29	2400	2.19	1.1	33
Packsand	18	15.40	21.6	2700	3.15	7.1	37
Siltstone	3	3.20	4.10	2500	2.56	1.8	28
Coal	10	0.37	0.54	1400	1.50	0.9	29
Siltstone	12	9.75	11.98	2500	2.56	3.1	30
Packsand	20	15.65	18.37	2700	3.15	6.5	35

Table 3
Mechanical properties of the fault.

Lithology	Shear (GPa)	Bulk (GPa)	Density ($kg \cdot m^{-3}$)	Cohesion (MPa)	Internal friction angle (°)	Tensile strength (MPa)
Fault	1.28	1.78	2000	0	30	0

To meet the objectives of the study, the thicknesses of the roof and floor of panel 2301N are adjusted. Considering the boundary effect, the coal pillars with a width of 100 m are maintained at both sides. Accordingly, a calculation model with dimensions of 600 m (length) × 122 m (high) is established as shown in Fig. 6. A hanging wall, footwall, and a fault zone are built because the model is cut by a normal fault [40]. In the mine-wide model, meshes are discretized more densely around the coal where the stopes are extracted compared to the meshes in the areas near the model boundary. Thus, the discretization method makes it possible to simulate a stress state in the active mining areas as accurately as possible within the available computation capability [34,40,41]. According to Jiang et al. [42], the roof rock is less sensitive to the density of the mesh; thus, the discretization method is deemed reasonable to ensure the convergence and stability of the simulation in this study. The main characteristics of the model are as follows. The thickness of the coal seam is 10 m, the dip angle of the normal fault is 45°, the fall height of the fault is 6 m, and the broken-belt width of the fault is 2 m.

The mechanical properties assigned to the blocks and joints of the model are conventionally derived from laboratory testing programs [43]. Table 2 lists the parameters of the main rock of the two fault walls derived from the geological report of panel 2301N and the rock mechanical test report of the borehole marked as 13–2S employed in the model. Because of the higher breakage and lower strength of the fault zone rock compared to the two fault walls, the parameters of the fault zone rock, presented in Table 3, are based on the previous studies and simulation experience [40,41,44]. The Mohr–Coulomb model is used to simulate the continuous part of the rock based on the elastic and plastic deformations of the overlying strata. The joint surface contact–Coulomb slip model is used to simulate the joint calculation [45]. According to Barton and Choubey [46], the basic friction angle of a typical rock joint falls into a range of 21–38°. Thus, in this study, it is considered to be 30°, which is an intermediate value in the range. For the Mohr–Coulomb failure criterion, the zero-cohesion and zero-tension are assumed because the strength of the fault or joint is generally quite low [47].

The full displacement constraint boundary is used for the bottom of the model. The horizontal displacement constraint and vertical displacement free are used at the left and right sides. The top boundary is free. The simulated depth of the coal seam is 700 m and the roof height of the model is 80 m. Hence, the failed simulation of the overlying strata with a height of 620 m is presumed to be the vertical stress acting on top of the model. Thus, the compensated load can be calculated using Eq. (4), as follows:

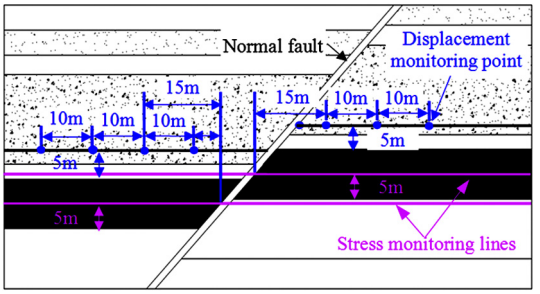

Fig. 7. Layout of the stress monitoring lines and displacement monitoring points of the working face.

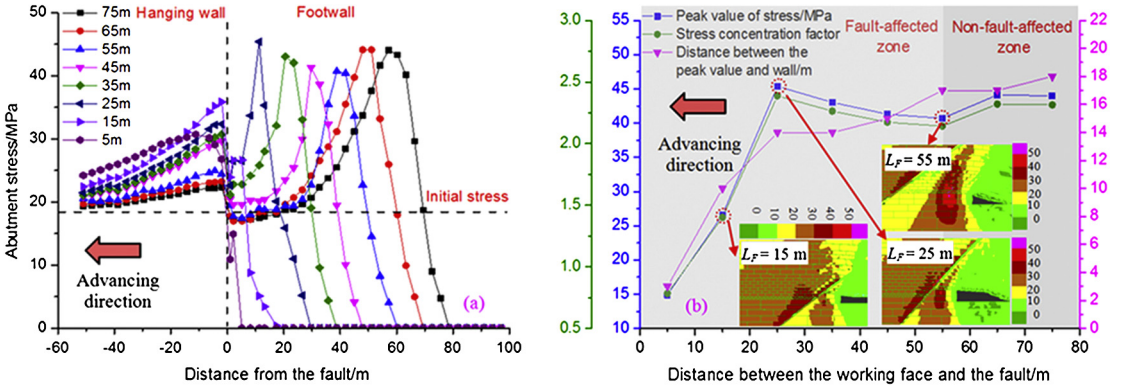

Fig. 8. Evolution of the front abutment stress during footwall mining. (a) Distribution of the front abutment stress, and (b) peak value and position of the abutment stress.

$$\sigma_v = \gamma h_v = 25.5\ \mathrm{kN\,m^{-3}} \times 620\ \mathrm{m} = 15.81\ \mathrm{MPa} \tag{4}$$

where γ and h_v are the unit weight of the rock mass and the height of the failed simulate strata, respectively. In the present study, the failed simulation height is 620 m, and the unit weight of the overlying rock mass is assumed to be 25.5 kN/m^3 [48].

Because the initial stress test is generally not conducted in many Chinese coalmines, including the Xinjulong coalmine, the lateral stress coefficient can be obtained using the empirical formulas or statistical formulas from previous studies. Kang et al. [49] define the lateral stress coefficient as the ratio of the two horizontal principal stresses to the vertical stress, which can be calculated using Eq. (5), as follows:

$$\lambda = 129.6/H_v + 0.5595 \tag{5}$$

where H_v is the depth of the coal seam (700 m). Thus, $\lambda = 0.74$. Based on the formation mechanism of the normal faults, $\lambda < 1$ because the vertical stress is the major principal stress. In addition, Brown and Hoek [50] proposed the following equation:

$$100/H_v + 0.3 \le \lambda \le 1500/H_v + 0.5 \tag{6}$$

The obtained variation range is $0.44 \le \lambda \le 2.64$. Therefore, the lateral stress coefficient $\lambda = 0.74$ is deemed reasonable.

3.2. Evolution laws of strata behaviors of working face affected by fault

When the working face approaches the fault, the distribution and peak values of the front abutment stress are notably affected by the fault. The roof rocks exhibits large-scaled movement. Hence, the studies conducted on the evolution laws of the abutment stress and the roof movement of the working face affected by the fault can serve as a reference for the prediction and prevention of rock bursts in the vicinity of the fault.

3.2.1. Evolution laws of abutment stress of working face

Two stress-monitoring lines are set up in the coal seam of the footwall and hanging wall (as shown in Fig. 7). The stress data are extracted with respect to different distances between the working face and the fault, which is in the range of 75–5 m with an interval of 10 m. Figs. 8 and 9 show the evolution laws of the front abutment stress of the working face.

As shown in Fig. 8, when the working face in the footwall advances toward the normal fault, the distance between the working face and the normal fault is in the range of 75–55 m, i.e. 75 m $\ge L_F \ge$ 55 m. The normal fault has negligible

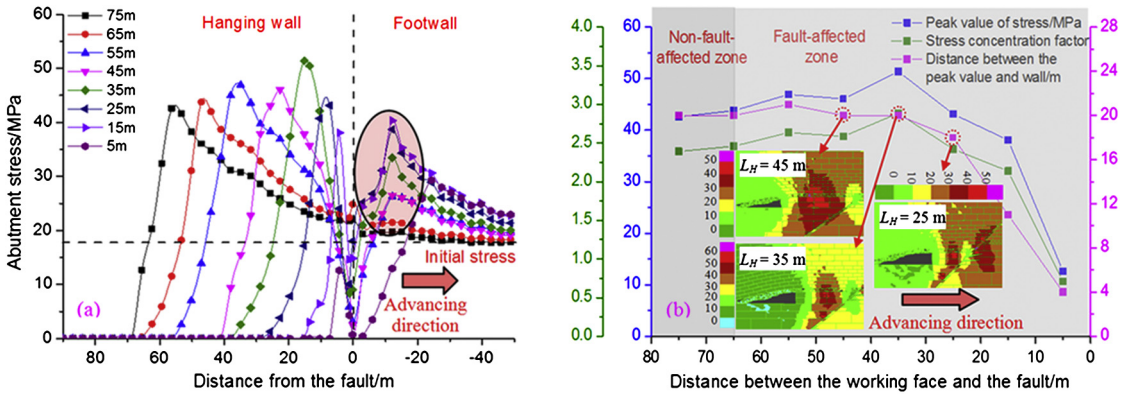

Fig. 9. Evolution of the front abutment stress during the hanging wall mining. (a) Distribution of the front abutment stress, and (b) peak value and its position of the abutment stress.

effect on the abutment stress because of the invariant distribution of the abutment stress of the working face; however, the abutment stress is high because of the large-scale suspension of the hard and thick main roof. In this study, when $L_F = 75$ m, the numerical simulation results indicate that the peak stress is 44 MPa (the in situ stress is 17.85 MPa), the stress concentration factor is 2.46, the distance between the stress peak value and the working face is 18 m, and the influence range of the stress is 42 m. The on-site observation results indicate that the distance between the stress peak value and the working face is 2–3.5 times the mining coal height (i.e. 10 m in this study), the stress concentration factor is in the range of 2.5–3, and the influence range of the stress is 40–60 m [13]. Thus, the results noted above are similar, thereby proving that the numerical simulation model is reasonable.

When 55 m $> L_F \geq$ 25 m, a large fault coal pillar is formed between the working face and the fault, and the integrity of the coal-rock mass is destroyed because of the fault cutting. Moreover, the stress concentration of the coal pillar is notable because of the block of the fault, which increases gradually as the working face advances toward the fault, attaining a maximum value of 45.38 MPa when $L_F = 25$ m. Hence, high-concentrated stress acts on the fault coal pillar. Subsequently, the strain energy is released because of the violent fracturing of the coal pillar or the intact rock.

When 25 m $> L_F \geq$ 5 m, the bearing capacity of the small-fault coal pillar decreases notably and the supported load on the coal pillar is small because of the fault cutting. Hence, the peak value of the abutment stress decreases to 14.90 MPa, and the distance between the peak value and the fault is 2 m when $L_F = 5$ m.

When the working face in the hanging wall advances toward the normal fault, the distance between the working face and the fault can be represented using L_H. From Fig. 9, when 55 m $\geq L_H \geq$ 35 m, because of the inverted-wedge-shaped overlying strata structure cut by the fault, the structure of the overlying strata is relatively stable. Thus, the concentrated stress of the coal pillar is high with a maximum value of 51.40 MPa when $L_H = 35$ m. The fault coal pillar is in the state of high-concentrated stress.

When 35 m $> L_H \geq$ 5 m, the bearing capacity decreases notably with the decrease in the width of the coal pillar. Hence, the abutment stress decreases to 12.61 MPa and the distance between the peak value and the fault is 2 m when $L_H = 5$ m.

3.2.2. Evolution laws of roof subsidence of working face

A displacement measuring point is installed on the roof with a height of 5 m over the coal wall with each working-face mining cycle (as shown in Fig. 7). After each mining cycle, the roof subsidence is recorded, and the deformation data is erased before the next mining cycle. The four mining states, which correspond to the distances of 35 m, 25 m, 15 m, and 5 m between the working face and the fault, are selected to understand the movement laws of the roof during the footwall and hanging wall mining.

From Fig. 10, when 35 m $\geq L_F \geq$ 25 m, the large coal pillar cut by the fault has a strong bearing capacity; hence, the roof subsidence values slightly increase from 0.25 m to 0.33 m. Moreover, the roof has a good stability. When 25 m $> L_F \geq$ 5 m, the coal-rock mass becomes unstable, causing subsidence because of the low bearing capacity and severe failure of the small coal pillar. Thus, the roof subsidence value increases to 1.79 m notably, with a lack of the stability.

When 35 m $\geq L_H \geq$ 15 m, the roof has a good stability because of the inverted-wedge-shaped strata structure. Hence, the roof subsidence values slightly increase from 0.20 m to 0.33 m with the decrease in the width of the coal pillar. When 15 m $> L_H$, the roof moves violently because of the low bearing capacity and severe failure of the small coal pillar. The roof subsidence value notably increases to 1.34 m.

3.3. Evolution laws of fault stability induced by mining

The rock bursts due to faults are related to the fault's stability. Hence, the analysis of the stress state of the fault plane and the relative subsidence of the two fault walls are necessary to study the laws of the fault stability induced by mining.

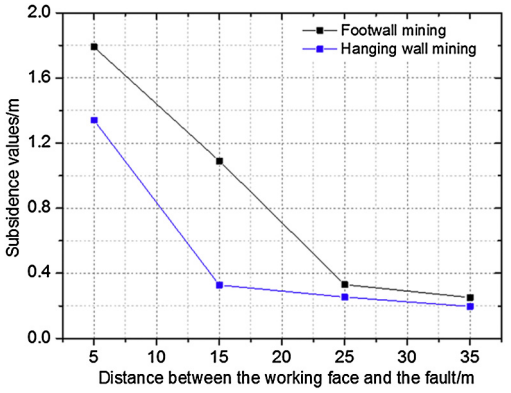

Fig. 10. Influence of the normal fault on the subsidence of roof over the coal wall.

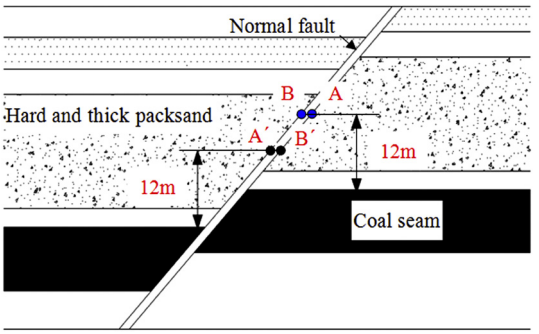

Fig. 11. Layout of the stress monitoring points of the fault plane.

Table 4
Stress monitoring data of fault plane.

Distance between the working face and the fault (m)	Footwall mining (point A)			Hanging wall mining (point A′)		
	Shear stress (MPa)	Normal stress (MPa)	Absolute values of the ratio of shear stress to normal stress	Shear stress (MPa)	Normal stress (MPa)	Absolute values of the ratio of shear stress to normal stress
45	1.46	−19.19	0.08	2.36	−26.76	0.09
35	0.97	−14.65	0.07	2.49	−25.04	0.10
25	1.36	−15.86	0.09	2.61	−22.76	0.11
15	0.45	−3.19	0.14	3.31	−21.59	0.15
5	2.60	−6.20	0.42	15.25	−21.56	0.71

3.3.1. Influence of mining on the stress of fault plane

The main roof of the hard and thick packs and with a thickness of 18 m is one of the main factors inducing fault rock bursts. Hence, two stress-monitoring points are setup on the interface between the main roof and the fault plane with a height of 12 m over the coal seam, which is marked as A (in the footwall) and A′ (in the hanging wall) as shown in Fig. 11. The normal stress and shear stress of the five mining states, which correspond to distances of 45 m, 35 m, 25 m, 15 m, and 5 m between the working face and the fault, are displayed in Table 4. These stresses can represent the stress state of the fault plane. However, fault activities cannot be directly established using the shear stress or the normal stress. Hence, the ratio of the shear stress to the normal stress can be employed [51,52]. The curves of the ratio of the shear stress to the normal stress are drawn, as shown in Fig. 12.

Fig. 12 shows that the variation curves of the ratio of the shear stress to the normal stress in the footwall mining or hanging wall mining are similar. The ratio is small and is invariant when 45 m $\geq L_F \geq$ 15 m or 45 m $\geq L_H \geq$ 15 m. The ratio increases notably when $L_F \leq$ 15 m or $L_H \leq$ 15 m. However, some differences in the stress state of the fault plane exist between the footwall mining and the hanging wall mining.

When 45 m $\geq L_F \geq$ 25 m, the normal stress is in the range of 14.65–19.19 MPa, and the shear stress is approximately 1 MPa. The normal stress and shears stress decrease notably when $L_F =$ 15 m because of the opening of the fault plane. When $L_F \leq$ 15 m, the normal stress and the shear stress increase, and the increasing amplitude of the latter is greater than the former. Thus, the ratio increases significantly, thereby increasing the possibility of fault activation.

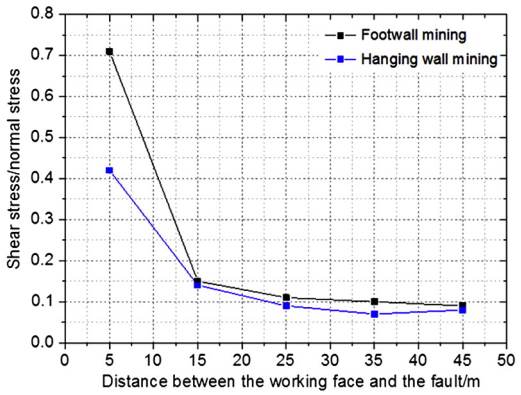

Fig. 12. Ratio variation of the fault plane stress affected by mining.

Table 5
Relative subsidence of the two fault walls.

Distance between the working face and the fault (m)		45	35	25	15	5
Footwall mining	Displacement of the point A (m)	−0.31	−0.33	−0.50	−1.76	−4.33
	Displacement of the point B (m)	−0.22	−0.25	−0.29	−0.86	−2.45
	Relative displacement (m)	0.09	0.08	0.21	0.91	1.88
Hanging wall mining	Displacement of the point A′ (m)	−0.13	−0.15	−0.18	−0.20	−0.48
	Displacement of the point B′ (m)	−0.02	−0.04	−0.05	−0.08	−0.13
	Relative displacement (m)	0.11	0.11	0.13	0.12	0.35

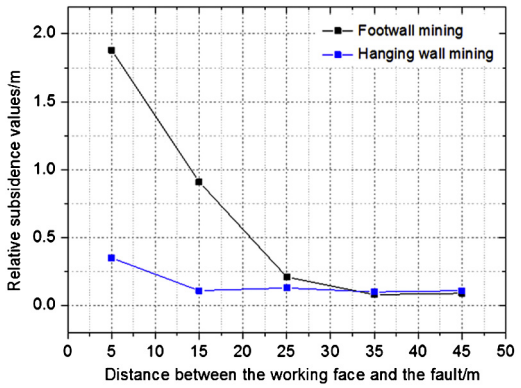

Fig. 13. Relative subsidence variation of the two fault walls affected by mining.

When 45 m $\geq L_H \geq$ 15 m, the normal and shear stresses are in the ranges of 22.76–26.76 MPa and 2.36–2.75 MPa, respectively. When $L_H <$ 15 m, the shear stress increases significantly and so does the ratio, thus increasing the possibility of fault activation. Hence, the increase in the shear stress due to mining may induce fault activation and slipping.

3.3.2. Influence of mining on the relative subsidence of the two fault walls

Mining operations decrease the stability of the fault and lead to fault slipping. Two adjacent displacement monitoring points on the fault plane with a height of 12 m over the coal seam (A and B during the footwall mining or A′ and B′ during hanging wall mining) are set up as shown in Fig. 11. The vertical displacements are recorded and relative subsidence values of the two fault walls, which represent the fault slipping values, are obtained as presented in Table 5 and Fig. 13.

From Fig. 13 and Table 5, when $L_F \geq$ 25 m and $L_H \geq$ 15 m, the relative subsidence values of the two fault walls are small and remain invariant. With the working face advancing further, the subsidence increases notably because of the fault slipping with a maximum value of 1.88 m when $L_F =$ 5 m and 0.35 m when $L_H =$ 5 m. They are approximately 9 and 3 times, respectively, with $L_F =$ 25 m and $L_H =$ 25 m. Here, the fault band and elastic rock system are in the unstable state, which will easily induce the rock burst.

Based on the comparative analysis of the two curves, the relative subsidence affected by the mining operations in the two fault walls is negligible when $L_F \geq$ 25 m and $L_H \geq$ 25 m. However, it increases notably when $L_F \leq$ 25 m and $L_H \leq$ 15 m, which implies that mining activity significantly affects the stability of the fault. Additionally, the maximum relative

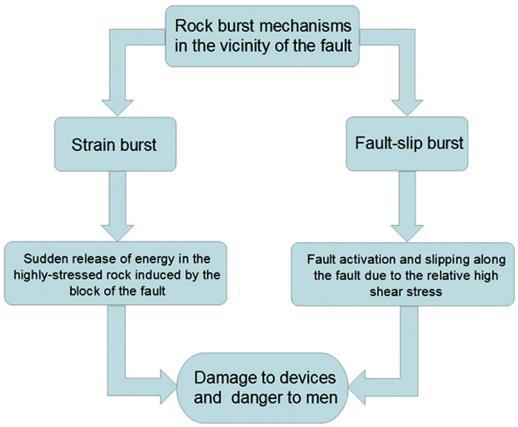

Fig. 14. Mechanisms of the rock burst near the fault [18].

Table 6
Peak values of the abutment stress with different fault dip angles.

Dip angle of the fault (°)		30	45	60	75	90
Peak values of abutment stress (MPa)	Footwall mining	47.79	45.38	44.20	54.22	72.25
	Hanging wall mining	59.81	51.40	47.42	55.05	73.36

subsidence value during hanging wall mining only accounts for 18.62% that of the footwall mining. This shows that the risk of rock bursts due to fault slipping during hanging wall mining is much lower than that during footwall mining.

3.4. Induced analysis of fault rock bursts due to mining

Based on the comprehensive analysis of the influence of the strata behaviors affected by the fault and the instability of the fault induced by the mining operation, the fault rock bursts can be induced by the high-concentrated stress acting on the fault coal pillar or by fault activation and slipping. Hence, based on the different inducing factors of rock bursts in the fault zone, the strain burst and fault-slip burst can be divided in the vicinity of the fault (in Fig. 14) [18] as follows.

When the fault coal pillar is large, a large amount of elastic strain energy is accumulated, and the high abutment stress concentrated in the coal pillar is due to the effect of the deadweight of the overlying strata and the block of the fault. This can easily induce strain burst, with the strain energy being released because of the violent fracturing of the coal pillar or the intact rock.

When the fault coal pillar is small, the stress state of the fault plane changes significantly and the ratio of the shear stress to the normal fault increases notably. The relative subsidence due to the slipping of the two fault walls increases significantly, which results in the sudden release of elastic energy of the fault band and elastic rock system. Hence, the fault-slip burst might be easily induced.

4. Numerical analysis on induced effect of dip angle of normal fault on rock bursts

Equation (3) shows that the fault dip angle has some influence on rock burst. Hence, based on the model with a fault dip of 45°, the evolution characteristics of the strata behaviors of the working face affected by the fault and the instability of the fault induced by the mining operations with different fault dip angles are analyzed. The influence laws of the normal fault with different dip angles on the rock burst are then revealed by changing the dip angle, i.e. 30°, 60°, 75°, and 90°, which are marked as $\theta = 30°$, 60°, 75°, and 90°, respectively.

4.1. Influence laws of fault dip angle on the abutment stress

The prerequisite for the rock burst to occur is the concentrated stress of the coal-rock mass exceeding its ultimate strength [53]. By comparing the distributions of the abutment stress during footwall mining or hanging wall mining with different dip angles of the normal fault, the nephograms of the abutment stress are obtained, as shown in Fig. 15, and its peak values are obtained, as displayed in Table 6. Fig. 15 shows that the distribution of the abutment stress is different according to the different dip angles of the normal fault.

From Fig. 16 and Table 6, when the working face in the footwall advances toward the normal fault with $\theta \leq 60°$, the overlying strata rotates to the goaf while the hanging wall is in the cantilever state. Hence, the overlying load on the coal pillar is small and the concentrated stress of the coal pillar is relatively low. When the fault has a large dip angle, the

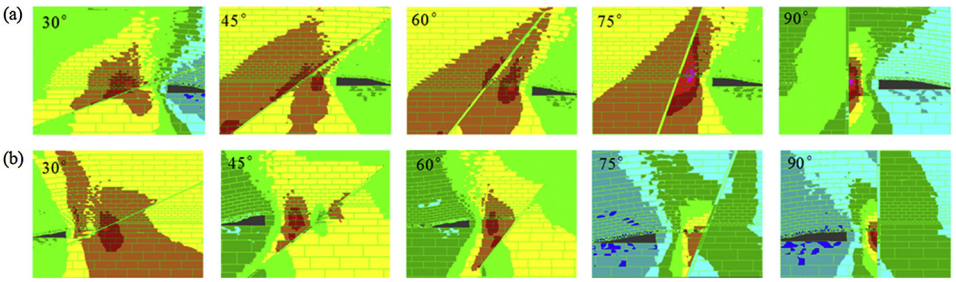

Fig. 15. Nephograms of the abutment stress with different fault dip angles of (a) footwall mining, and (b) hanging wall mining.

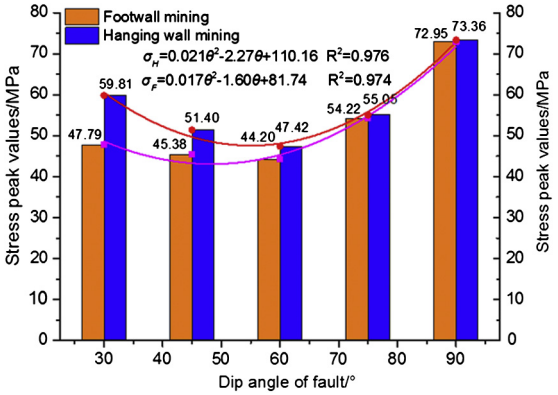

Fig. 16. Peak values of the abutment stress influenced by the fault dip angle.

concentrated stress of the coal pillar increases because of the increase in the overlying load acting on the coal pillar. The peak value of the abutment stress is 72.95 MPa when $\theta = 90°$.

During the hanging wall mining, the overlying strata are relatively stable because of the inverted-wedge-shaped structure, which results in considerable stress concentration. When the fault has a small dip angle, roof stability is better and stress concentration is higher. Moreover, the abutment stress is 59.81 MPa with $\theta = 30°$. The roof stability becomes worse and the stress concentration reduces with the increase in the dip angle of the fault. When the fault has a large dip angle, the roof stability is worse, and the concentrated stress of the coal-rock mass increases because of the tendency of the roof slipping along the fault plane. The peak value of the abutment stress is 73.36 MPa when $\theta = 90°$.

The comparative analysis of the two curves shows that the difference in the stress peak values between the two fault walls decreases gradually with the increase in the fault dip angle, and it is negligible when $\theta = 90°$. Hence, the larger the fault dip angle, the lesser is the influence on the stress peak values of the working face in the two fault walls.

The relationship between the peak values of the abutment stress and the fault dip angle can be obtained by curve fitting as shown in Eqs. (7) and (8). The fitting accuracy of the two curves is high.

Footwall mining:

$$\sigma_{\mathrm{F}} = 0.017\theta^2 - 1.60\theta + 81.74\, R^2 = 0.974 \tag{7}$$

Hanging wall mining:

$$\sigma_{\mathrm{H}} = 0.021\theta^2 - 2.27\theta + 110.16\, R^2 = 0.976 \tag{8}$$

Therefore, it can be concluded that the possibility of the strain burst is different for different fault dip angles. Regardless of whether it is the footwall mining or the hanging wall mining, the abutment stress of the coal pillar with a large fault dip angle is higher than that with a small dip angle. Hence, the possibility of the strain burst with a large fault dip angle is greater than that with a small dip angle.

4.2. Influence laws of fault stability induced by mining with different fault dip angles

Based on the comparative analysis of the stress state of the fault plane and the relative subsidence values of the two fault walls, the comprehensive contrast results of the influence of mining on the stability of the fault is more obvious when the distance between the working face and the fault is in the range of 5–15 m. Hence, the faults are considered at a distance of 15 m with respect to the different fault dip angles in this study.

Table 7
Stress monitoring data of fault plane with different fault dip angles.

Dip angle of the fault (°)	Footwall mining (point A)			Hanging wall mining (point A′)		
	Shear stress (MPa)	Normal stress (MPa)	Absolute values of the ratio of shear stress to normal stress	Shear stress (MPa)	Normal stress (MPa)	Absolute values of the ratio of shear stress to normal stress
30	0.0021	−0.032	0.07	2.94	−26.51	0.11
45	0.45	−3.19	0.14	3.31	−21.59	0.15
60	12.64	−25.48	0.50	5.92	−13.99	0.42
75	19.01	−29.85	0.64	7.79	−29.79	0.26
90	4.19	−20.99	0.20	3.45	−20.53	0.17

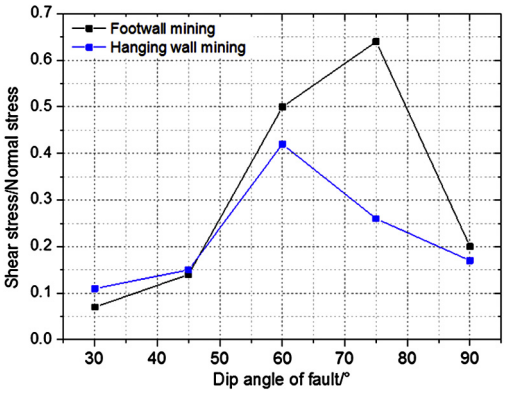

Fig. 17. Ratio variation in the fault plane stress affected by mining with different fault dip angles.

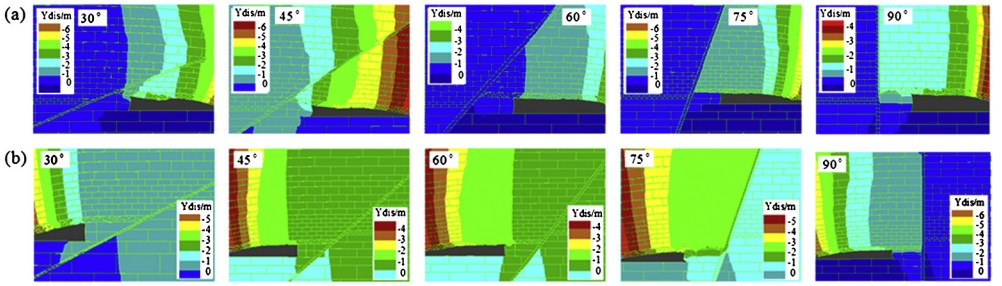

Fig. 18. Nephograms of the vertical displacement with different fault dip angles. (a) Footwall mining, and (b) hanging wall mining.

4.2.1. Influence of mining on the stress state of fault with different dip angles

The normal stress and shear stress of points A and A′ on the fault plane with different fault dip angles are obtained when the distance between the working face and the fault is 15 m and displayed in Table 7. Fig. 17 shows the two curves of the ratio of the shear stress to the normal stress.

As shown in Fig. 17, when the dip angle of the fault is small, the ratio of the shear stress to the normal fault is low. However, the normal and shear stresses are low during footwall mining because of loosening and opening of the fault plane, while the stresses are high during hanging wall mining because the fault plane is less affected by mining. The ratio of the shear stress to the normal fault increases and the increasing magnitude of the latter is greater than the former, with a larger fault dip angle, which increases the possibility of fault activation. The maximum value of the ratio during the footwall mining is 0.64 with $\theta = 75°$, while that during the hanging wall mining is 0.42 with $\theta = 60°$. As the dip angle continues to increase, the normal and shear stresses decrease and the decreasing amplitude of the latter is greater than that of the former. Hence, the ratio of the shear stress to the normal stress decreases significantly, thus reducing the possibility of fault activation.

Hence, it can be concluded that in both footwall mining and hanging wall mining, the possibility of fault activation with a large fault dip angle is greater than that with a small dip angle, indicating that the possibility of the fault-slip burst is higher.

4.2.2. Influence of mining on relative subsidence of the two fault walls with different dip angles

Fig. 18 shows the nephograms of the vertical displacement with different fault dip angles. The displacement values of points A and B during footwall mining or points A′ and B′ during hanging wall mining are recorded. The relative subsidence

Table 8
Relative subsidence of the two fault walls with different dip angles of the normal fault.

Dip angle of the fault (°)		30	45	60	75	90
Footwall mining	Displacement of the point A (m)	−2.69	−1.76	−0.66	−1.21	−1.10
	Displacement of the point B (m)	−1.67	−0.86	−0.23	−0.11	−0.03
	Relative displacement (m)	1.02	0.91	0.43	1.10	1.07
Hanging wall mining	Displacement of the point A′ (m)	−0.12	−0.20	−0.49	−2.27	−1.53
	Displacement of the point B′ (m)	−0.06	−0.08	−0.02	−0.03	−0.03
	Relative displacement (m)	0.06	0.12	0.47	2.24	1.50

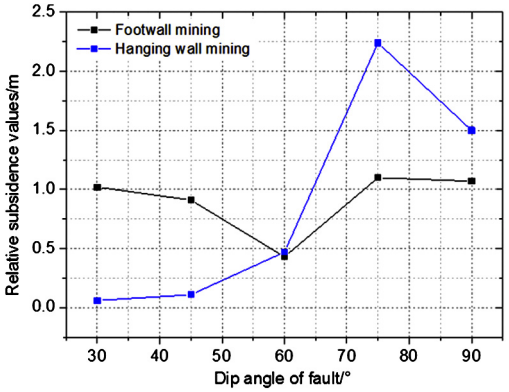

Fig. 19. Relative subsidence variation in the two fault walls affected by mining with different fault dip angles.

values of the two fault walls are then calculated. Table 8 lists the results. The curves of the relative subsidence with different fault dip angles are then obtained, as shown in Fig. 19.

As shown in Fig. 19, during footwall mining with a fault state of $\theta \leq 45°$, the relative subsidence is larger because the fault opens. With the increase in the dip angle, the relative subsidence reduces because the effect of mining on the roof is less. However, the fault-slipping effect is notable and the relative subsidence due to the fault slipping is 0.43 m with $\theta = 60°$, which might induce a fault-slip burst. If $\theta \geq 60°$, the subsidence of the footwall strata increases notably because of the large slipping effect, whereas the subsidence of the roof on the hanging wall can be neglected. Hence, the relative subsidence increases significantly with a maximum value of 1.10 m when $\theta = 75°$. Moreover, the fault band and elastic rock system are unstable, thus increasing the possibility of fault slip.

During hanging wall mining with a fault state of $\theta \leq 60°$, the subsidence of the two fault walls is small because the fault plane is less affected by mining activities. Hence, the relative subsidence remains invariant. If $\theta \geq 60°$, the subsidence of the hanging wall strata increases significantly because of the large slipping effect, while the subsidence of the footwall strata is negligible. Thus, the relative subsidence increases significantly with a maximum value of 2.24 m when $\theta = 75°$. Moreover, the fault band and elastic rock system are unstable, which might lead to a fault-slip burst.

Therefore, it can be concluded that in both footwall mining and the hanging wall mining, the ratio of the shear tress to the normal stress of the fault plane and the relative subsidence of the two fault walls due to the fault slipping effect with a large fault dip angle are higher than that with a small dip angle. Hence, fault-slip bursts are easily induced with a large fault dip angle compared to a small dip angle.

5. Engineering case

The panel $103_{down}03$ is the third working face of the coal seam marked as 3_{down} in the 10th district of the coalmine in Shandong province. The average mining depth is 521 m, and the strike length and the length of the working face are in the ranges of 1293–1594 m and 108–190 m, respectively. The northern side of panel $103_{down}03$ is the goaf of $103_{down}02$. The south side is the coal body of $103_{down}04$. The upper side is the goafs of $103_{up}02$ and $103_{up}03$. Fig. 20 shows the position of panel $103_{down}03$. The average thickness and dip angle of the coal seam are 3.26 m and 8°, respectively. The hardness is 3.1, representing a strong bursting liability. The lithologies of the roof and floor of the working face are largely sandstone. Based on the on-site materials, two normal faults marked as X-F19 (dip angle of 58° and fall height of 3.2 m) and X-F20 (dip angle of 30° and fall height of 0.8 m) significantly affect the mining of panel $103_{down}03$.

The mining on panel $103_{down}03$ commenced on June 12, 2011 and the mining activity were completed on March 15, 2012. The seismological observation system (SOS) developed by the Poland Central Mining Institute was installed and operated during the mining of the working face. The microseismic signal provides real-time monitoring for energy signals exceeding 10^2 J. The measurement accuracy is greater than 97%. Many microseismic events are monitored during the min-

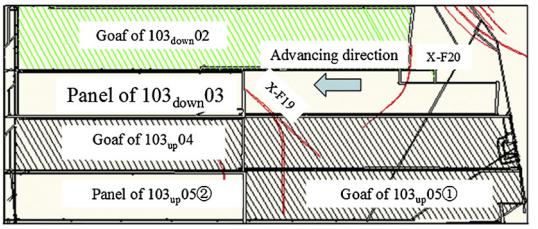

Fig. 20. Plan of panel $103_{down}03$.

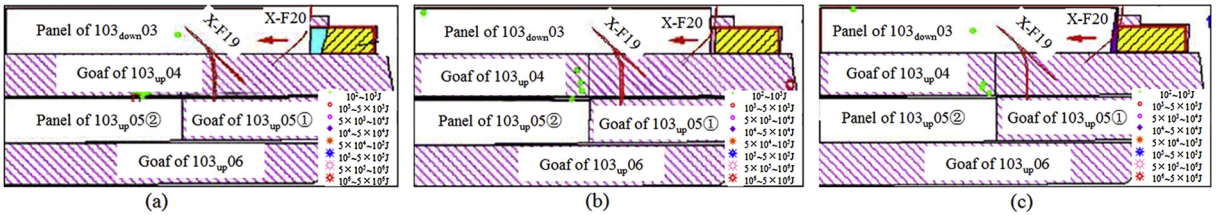

Fig. 21. Planar distribution of microseismic events during the 7/24–8/14 of panel $103_{down}03$. (a) 7/24–7/31, (b) 8/1–8/7, and (c) 8/7–8/14.

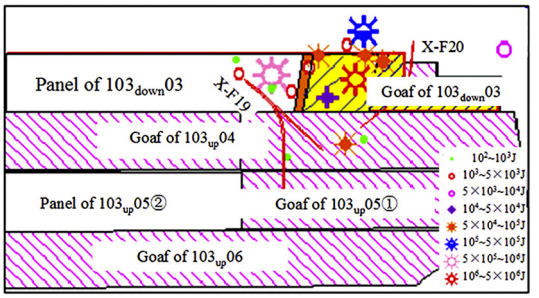

Fig. 22. Planar distribution of microseismic events during the 9/26–10/2 of panel $103_{down}03$.

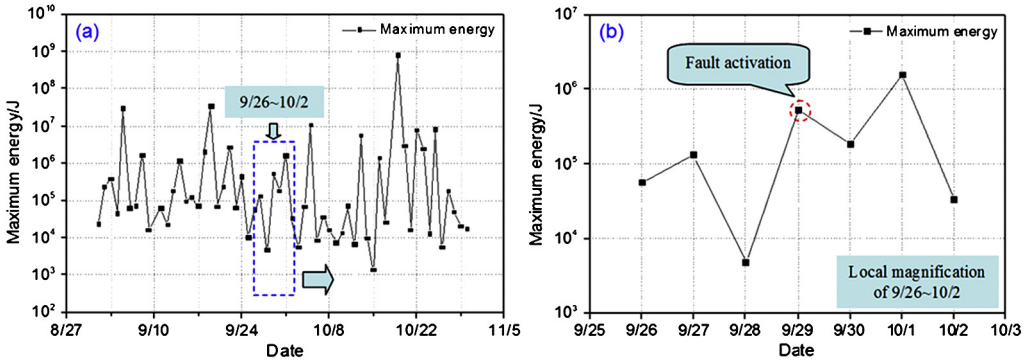

Fig. 23. Maximum energy microseismic events of panel $103_{down}03$. (a) 9/1–10/30, and (b) 9/26–10/2.

ing of the working face. Therein, an event with high energy exceeding 10^5 J occurred near the fault of X-F19 and the vibration was notable in the working face.

Hence, based on the SOS monitoring data, the microseismic events that were monitored when the working face approaches X-F20 and X-F19 during the period from July 24, 2011 to August 14, 2011 and the period from September 26, 2011 to October 2, 2011 are selected and analyzed to study the distributions and energy of the microseismic activities, as shown in Figs. 21 and 22, respectively. When the working face approaches the fault of X-F20, the number of microseismic events is few and the corresponding energy is low. However, the number of microseismic events is higher when the working face approaches the fault of X-F19, and a shock bump with energy levels of 535142.1 J occurs in the vicinity of the fault on September 26, 2011 (Figs. 22 and 23). The primary reason based on the filed data is that the fault stops the transmission of the stress, and the fault activation and slipping induced by the concentrated stress leads to energy release and shock bump.

Mining on panel $103_{down}03$ commenced from the footwall. Hence, based on the dip angle of the fault and referring to the influence laws of the fault stability induced by mining, given in Section 4.2, it can be concluded that the stress state and the relative subsidence of the fault with different fault dip angles are significantly affected by mining on the footwall. Moreover, the relative subsidence due to the fault-slipping effect with a large fault dip angle is more pronounced than that with a small dip angle, which is affected by fault opening. Therefore, the strata behaviors induced by fault slipping in the vicinity of the X-F19 are more violent than that of the small fault dip angle of X-F20. The fault-slip burst is much easily induced. However, it should be noted that the rock bursts near the fault are induced because of the combination of multiple factors, and the fault dip angle is only one of the references.

6. Conclusions

In this study, the evolution laws of the strata behaviors of the working face affected by a fault and the instability of the fault with the advancement of the working face toward a normal fault are analyzed to investigate the mechanism inducing rock bursts and the influence characteristics of the fault dip angle. A numerical model is generated using UDEC software.

It can be concluded that when the fault coal pillar is large, a large amount of elastic strain energy is accumulated and the abutment stress is highly concentrated in the coal pillar under the effects of the deadweight of the overlying strata and the block of the fault. Thus, a strain burst can be easily induced with the release of strain energy because of the violent fracturing of the coal pillar or the intact rock. When the fault coal pillar is small, the stress state of the fault plane changes significantly, and the ratio of the shear stress to the normal fault increases. Moreover, the relative subsidence of the two fault walls due to the fault slipping increase remarkably, resulting in the sudden release of elastic energy of the fault band and elastic rock system. Hence, the fault-slip burst is easily induced. In both the footwall mining and hanging wall mining, the possibility of the strain burst with a large dip angle is greater than that with a small dip angle. This is because the abutment stress of the coal pillar with a large dip angle of the fault is higher than that with a small dip angle. In addition, the ratio of the shear tress to the normal stress of the fault plane and the relative subsidence of the two fault walls induced by the fault-slipping effect with a large fault dip angle are higher than that with a small dip angle. Hence, the fault-slip burst can be easily induced with a large fault dip angle. Finally, a case of the microseismic events is used to verify the results of the numerical simulation.

The results used to analyze the mining effects under the influences of the normal faults and dip angles are significant for the prediction and prevention of rock bursts.

Acknowledgements

The study was supported by the National Natural Science Foundation of China (Grant No. 51574155), the Tai'an Science and Technology Development Plan of Shandong Province (Grant No. 2015ZC1058), the Science and Technology Innovation Fund of College of the Mining and Safety Engineering, Shandong University of Science and Technology (Grant No. KYKC17008), the State Key Laboratory for GeoMechanics and Deep Underground Engineering, China University of Mining and Technology (Grant No. SKLGDUEK1725), and State Key Laboratory for Mining Disaster Prevention and Control (Grant No. MDPC201602) and research funding (Grant No. J17KA212) from Government of Shandong Province.

References

[1] E.J. Sellers, P. Klerck, Modelling of the effect of discontinuities on the extent of the fracture zone surrounding deep tunnels, Tunn. Undergr. Space Technol. 15 (4) (2000) 463–469.
[2] P. Wang, J.Q. Jiang, P.P. Zhang, Q.L. Wu, Breaking process and mining stress evolution characteristics of a high-position hard and thick stratum, Int. J. Min. Sci. Technol. 26 (4) (2016) 563–569.
[3] T. Li, Z.L. Mu, G.J. Liu, J.L. Du, H. Lu, Stress spatial evolution law and rockburst danger induced by coal mining in fault zone, Int. J. Min. Sci. Technol. 26 (3) (2016) 409–415.
[4] Y.L. Rebetsky, Achievements of tectonophysics research in Russia: present status and perspective, C. R. Géoscience 344 (3–4) (2012) 116–124.
[5] S.R. Wang, N. Li, C.L. Li, Z.S. Zou, X. Chang, Instability mechanism analysis of pressure-arch in coal mining field under different seam dip angles, Dyna (Bilbao) 90 (2015) 279–284.
[6] G. Swift, Relationship between joint movement and mining subsidence, Bull. Eng. Geol. Environ. 73 (73) (2014) 163–176.
[7] W.C. Zhu, Z.H. Li, L. Zhu, C.A. Tang, Numerical simulation on rockburst of underground opening triggered by dynamic disturbance, Tunn. Undergr. Space Technol. 25 (5) (2010) 587–599.
[8] Z.A. Zhou, Normal fault causing coal bed thin and thick and "reversed-drag" normal fault, Bull. Inst. Geomech. CAGS (1985) 107–114.
[9] Y.F. Zeng, S.Q. Liu, W. Zhang, Y.L. Zhai, Application of artificial neural network technology to predicting small faults and folds in coal seams, China, Sustain. Water Resour. Manag. 2 (2) (2016) 175–181.
[10] T.G. Blenkinsop, Relationships between faults, extension fractures and veins, and stress, J. Struct. Geol. 30 (5) (2008) 622–632.
[11] D.J. Gates, P. Hornby, K.B. Mckenzie, A mechanical theory of normal fault orientation, Eng. Geol. 38 (1–2) (1994) 35–52.
[12] Z.H. Li, L.M. Dou, Z.L. Mu, A.Y. Cao, S.Y. Gong, Y.G. Wang, Effect of fault on roof rock burst, J. Min. Saf. Eng. 25 (2) (2008) 154–158,163.
[13] X.H. Chen, W.Q. Li, X.Y. Yan, Analysis on rock burst danger when fully-mechanized caving coal face passed fault with deep mining, Saf. Sci. 50 (4) (2012) 645–648.
[14] A.F. Durand, E.A. Eargas Jr., L.E. Vaz, Applications of numerical limit analysis (NLA) to stability problems of rock and soil masses, Int. J. Rock Mech. Min. Sci. 43 (3) (2006) 408–425.
[15] Z.P. Meng, S.P. Peng, H. Li, Influence of normal faults on the physical and mechanical properties of coal and the distribution of underground pressure, J. China Coal Soc. 26 (6) (2001) 561–566.

[16] W. Müller, Numerical simulation of rock bursts, Min. Sci. Technol. 12 (1) (1991) 27–42.
[17] J.W. Shi, Z.L. Chen, Based on numerical simulation study of rockburst in roadway induced by fault, Adv. Mater. Res. 962–965 (2014) 370–374.
[18] A. Sainoki, H.S. Mitri, Dynamic behaviour of mining-induced fault slip, Int. J. Rock Mech. Min. Sci. 66 (1) (2014) 19–29.
[19] H.G. Ji, H.S. Ma, J.A. Wang, Y.H. Zhang, H. Cao, Mining disturbance effect and mining arrangements analysis of near-fault mining in high tectonic stress region, Saf. Sci. 50 (4) (2012) 649–654.
[20] Y.D. Jiang, T. Wang, Y.X. Zhao, C. Wang, Numerical simulation of fault activation pattern induced by coal extraction, J. China Univ. Min. Technol. 42 (1) (2013) 1–5.
[21] Z.H. Li, L.M. Dou, Z.Y. Lu, X.W. Lu, G.R. Wang, Study of the fault slide destabilization induced by coal mining, J. Min. Saf. Eng. 27 (4) (2010) 499–504.
[22] X.P. Lai, P.F. Shan, J.T. Cao, F. Cui, H. Sun, Simulation of asymmetric destabilization of mine-void rock masses using a large 3D physical model, Rock Mech. Rock Eng. 49 (2) (2016) 487–502.
[23] T.B. Li, X.F. Wang, L.B. Meng, A physical simulation test for the rockburst in tunnels, J. Mt. Sci. 8 (2) (2011) 278–285.
[24] Z.L. Li, L.M. Dou, W. Cai, G.F. Wang, H. Jiang, S.Y. Gong, Y.L. Ding, Investigation and analysis of the rock burst mechanism induced within fault–pillars, Int. J. Rock Mech. Min. Sci. 70 (9) (2014) 192–200.
[25] S.P. Peng, Z.P. Meng, Y.L. Li, Influence of faults on coal roof stability by physical modeling study, Coal Geol. Explor. 29 (3) (2001) 1–4.
[26] A.W. Wang, Y.S. Pan, Z.H. Li, C.S. Liu, R.J. Han, X.F. Lv, H.Q. Lu, Similar experimental study of rockburst induced by mining deep coal seam under fault action, Rock Soil Mech. 35 (9) (2014) 2486–2492.
[27] W. Gong, Y.Y. Peng, H. Wang, M.C. He, L. Sousa, Fracture angle analysis of rock burst faulting planes based on true-triaxial experiment, Rock Mech. Rock Eng. 48 (3) (2015) 1017–1039.
[28] Z.L. Li, L.M. Dou, W. Cai, G.F. Wang, H. Jiang, Y.L. Ding, Y. Kong, Mechanical analysis of static stress within fault-pillars based on a voussoir beam structure, Rock Mech. Rock Eng. 49 (3) (2016) 1097–1105.
[29] Y. Pan, Y. Liu, S.F. Gu, Fold catastrophe model of mining fault rockburst, Chin. J. Rock Mech. Eng. 20 (1) (2001) 43–48.
[30] X.B. Wang, Y.S. Pan, L. Hai, Instability criterion of fault rockburst based on gradient-dependent plasticity, Chin. J. Rock Mech. Eng. 23 (4) (2004) 588–591.
[31] Y.L. Huang, J.X. Zhang, B.F. An, Q. Zhang, Overlying strata movement law in fully mechanized coal mining and backfilling longwall face by similar physical simulation, J. Min. Sci. 47 (2011) 618–627.
[32] W.B. Xie, X.X. Chen, B.S. Zheng, Numerical Simulation Research and Analysis of Mining Engineering Problem, China University of Mining and Technology Press, Xuzhou, 2005.
[33] D.W. Zhou, K. Wu, G.L. Cheng, L. Li, Mechanism of mining subsidence in coal mining area with thick alluvium soil in China, Arab. J. Geosci. 8 (2014) 1855–1867.
[34] A. Sainoki, H.S. Mitri, Methodology for the interpretation of fault-slip seismicity in a weak shear zone, J. Appl. Geophys. 110 (2014) 126–134.
[35] M. Bischoff, A. Cete, R. Fritschen, T. Meier, Coal mining induced seismicity in the Ruhr area, Germany, Pure Appl. Geophys. 167 (1) (2010) 63–75.
[36] B. Domański, S.J. Gibowicz, Comparison of source parameters estimated in the frequency and time domains for seismic events at the Rudna copper mine, Poland, Acta Geophys. 56 (2) (2008) 324–343.
[37] S.T. Zhu, F.X. Jiang, K.J.A. Kouame, X.F. Li, W.F. Tan, B. Zhang, H. Zhang, Fault activation of fully mechanized caving face in extra-thick coal seam of deep shaft, Chin. J. Rock Mech. Eng. 35 (1) (2016) 50–58.
[38] J. Coggan, F.Q. Gao, D. Stead, D. Elmo, Numerical modelling of the effects of weak immediate roof lithology on coal mine roadway stability, Int. J. Coal Geol. 90–91 (1) (2012) 100–109.
[39] S. Shnorhokian, H.S. Mitri, D. Thibodeau, Numerical simulation of pre-mining stress field in a heterogeneous rockmass, Int. J. Rock Mech. Min. Sci. 66 (9) (2014) 13–18.
[40] A. Sainoki, H.S. Mitri, Evaluation of fault-slip potential due to shearing of fault asperities, Can. Geotech. J. 52 (2015) 1417–1425.
[41] G.F. Hofmann, L.J. Scheepers, Simulating fault slip areas of mining induced seismic tremors using static boundary element numerical modeling, Trans. Inst. Min. Metall. 120 (1) (2015) 53–64.
[42] L.S. Jiang, A. Sainoki, H.S. Mitri, N.J. Ma, H.T. Liu, Z. Hao, Influence of fracture-induced weakening on coal mine gateroad stability, Int. J. Rock Mech. Min. Sci. 88 (2016) 307–317.
[43] W. Wang, Y.P. Cheng, H.F. Wang, H.Y. Liu, L. Wang, W. Li, J.Y. Jiang, Fracture failure analysis of hard-thick sandstone roof and its controlling effect on gas emission in underground ultra-thick coal extraction, Eng. Fail. Anal. 54 (2015) 150–162.
[44] F.H. Ma, L. Sun, D. Li, Numerical simulation analysis of covering rock strata as mining steep-inclined coal seam under fault movement, Trans. Nonferr. Met. Soc. China 21 (S3) (2011) 556–561.
[45] Itasca, Universal Distinct Element Code User's Guide (Version 4.0), Itasca Consulting Group, Minneapolis, 2005.
[46] N. Barton, V. Choubey, The shear strength of rock joints in theory and practice, Rock Mech. 10 (1977) 1–54.
[47] A. Sainoki, H.S. Mitri, Dynamic modelling of fault-slip with Barton's shear strength model, Int. J. Rock Mech. Min. Sci. 67 (6) (2014) 155–163.
[48] G. Herget, Stress assumptions for underground excavations in the Canadian shield, Int. J. Rock Mech. Min. Sci. Geomech. Abstr. 24 (1) (1987) 95–97.
[49] H.P. Kang, J. Lin, L.X. Yan, X. Zhang, Y.Z. Wu, L.P. Si, Study on characteristics underground in-situ stress distribution in Shanxi coalmine fields, Chin. J. Geophys. 52 (7) (2009) 1782–1792.
[50] E.T. Brown, E. Hoek, Trends in relationships between measured in-situ, stresses and depth, Int. J. Rock Mech. Min. Sci. Geomech. Abstr. 15 (4) (1978) 211–215.
[51] S.M. Yang, N.B. Zhang, J. Liu, S.K. Zhao, Research on mechanism of fault rock burst, Coal Sci. Technol. 42 (10) (2014) 6–9, 27.
[52] Z.H. Li, L.M. Dou, C.P. Lu, Z.L. Mu, A.Y. Cao, Study on fault induced rock bursts, Int. J. Min. Sci. Technol. 18 (3) (2008) 321–326.
[53] Z.H. Li, Research on Rockburst Mechanism Induced by Fault Slip During Coal Mining Operation, Ph.D. thesis, China University of Mining and Technology, Beijing, China, 2009.